Results in Engineering 23 (2024) 102405

Contents lists available at ScienceDirect

Results in Engineering

journal homepage: www.sciencedirect.com/journal/results-in-engineering

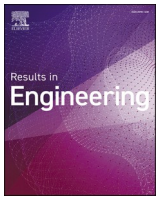

Crystal plasticity analysis of fatigue crack initiation site considering crystallographic orientation in Ti–22V–4Al alloy

Jinta Arakawa *, Koki Hirazumi, Takeshi Uemori **, Yoshito Takemoto

Graduate School of Natural Science and Technology, Okayama University, 3-1-1 Tsushimanaka, Kita-ku, Okayama, 700-8530, Japan

A R T I C L E I N F O

Keywords:
β-Ti
Fatigue crack initiation
Schmidt factor
Crystal plasticity FEM
Polycrystalline

A B S T R A C T

In this study, plane bending fatigue tests were conducted on Ti–22V–4Al alloy, a β-type titanium alloy, to examine the fatigue crack initiation behavior in detail. In addition, the prediction of fatigue crack initiation points was investigated from the perspectives of the Schmidt factor (SF) and crystal plasticity finite element method (CP-FEM). The slip system contributing to fatigue crack initiation can be accurately predicted by assessing the magnitude relationship of SF. Also, this prediction is already indicated in a lot of paper by using out of component of slip activity. However, the location where the fatigue crack will occur can be not estimated by SF on polycrystalline. Therefore, prediction of grains where fatigue cracks will occur could be achieved with high accuracy by constructing a CP-FEM that considers the mechanical interaction of polycrystals and grain boundary. Utilizing advanced methodologies such as CP-FEM and numerical calculation techniques, it is strictly investigated that the factors influencing fatigue crack initiation in polycrystalline materials. Our research concluded the understanding of fatigue crack initiation on polycrystal grains by considering the mechanical interaction of polycrystals and grain boundary.

1. Intoduction

Industrial α+β titanium alloys are difficult to machine due to the presence of the α phase, which hinders their application in small precision parts. Therefore, to significantly improve workability, a β-type titanium alloy consisting solely of the β phase was developed. This alloy exhibits high strength and excellent workability [1–5], making it widely used in aircraft landing gear and artificial hip joints [6–8]. Additionally, DAT51 (Ti–22V–4Al) is widely recognized as a common industrial β-type titanium alloy. This alloy can have a single-phase β (bcc structure) microstructure by adding a bit of amounts of V (vanadium) and Al (aluminum) and subjecting it to appropriate heat treatment microstructure [9,10]. With regard to β-type titanium alloy (Ti–22V–4Al), Tokaji et al. [11] investigated the effect of grain size on fatigue strength by changing the grain size of the same material. The results revealed a slight improvement in fatigue strength with decreasing grain size. Additionally, fracture surfaces (facets) were observed at the starting points of fatigue cracks in all specimens. It was observed that fatigue life can be standardized regardless of grain size by calculating the stress intensity factor range from the stress applied to the same position of these facets. In addition, Proudhon et al. [12], conducted a crystal plasticity finite element analysis of the near β-type titanium alloy VST55531 using cyclic stress-strain relationships and crystal orientations obtained from experiments. The findings revealed that micro fatigue cracks in the same material repeatedly propagate and bend along the {110} plane. Abdellah et al. [13], used CT specimens for Ti–27Nb to experimentally and analytically evaluate fatigue crack propagation paths. As a result, the crack propagation path can be accurately predicted by employing X-FEM using experimentally determined Paris law material constants C and m. Also, the results of evaluating slip systems which generate the fatigue crack are reported in many research papers. For example, Conghui Liu et al. [27], predicted the slip systems which generated the fatigue crack on near-alpha titanium alloy, by F parameter considering maximum Schmid factor (SF), the angle α between a loading direction and normal slip plane, and the angle Ω between a Burgers vector and specimen surface. As a result, it was found that the slip system generating the fatigue crack can be evaluated high accuracy based on F parameter. Furthermore, Fanchao Meng et al. [28], observed and evaluated the micro fatigue crack initiation and propagation on TiB/-near α-Ti Composite by using SF. The results indicated the micro fatigue crack propagated thorough the grains with utilizing the slip systems

* Corresponding author.
** Corresponding author.
E-mail address: jarakawa@okayama-u.ac.jp (J. Arakawa).

https://doi.org/10.1016/j.rineng.2024.102405
Received 30 March 2024; Received in revised form 29 May 2024; Accepted 11 June 2024
Available online 16 June 2024

Numencleature:

SF	Schmid factor
α	Angle between the slip line and the direction perpendicular to the load axis
β	Rotation angle for slip plane to normal axis of specimen surface
γ	Angle between the slip line and direction
Ω	Angle between the slip direction and specimen surface
Φ	Angle between the load axis and the normal direction of the slip surface
λ	Angle between the load axis and the slip direction
τ	Resolved shear stress (RSS)
F	Deformation gradient tensor
F*	Deformation gradient tensors in elastic
Fp:	Deformation gradient tensors in plastic
I	second-order unit tensor
F^{p}_{new}:	Plastic deformation gradient tensors after deformation
F^{p}_{old}:	Plastic deformation gradient tensors before deformation
$s_0^{(\alpha)}$:	Unit vector in the slip direction
$m_0^{(\alpha)}$:	Unit vector in the direction normal to the slip
$\dot{\gamma}^{(\alpha)}$:	Shear strain rate
$\dot{\gamma}_0^{(\alpha)}$:	Reference shear strain rate
$\tau^{(\alpha)}$:	RSS on slip system of α
$g^{(\alpha)}$:	Critical RSS (CRSS)
$g_0^{(\alpha)}$:	Initial value of the CRSS
k	Material constant
n	Material constant
C_{ij}	Elastic constants
σ_a	Stress amplitude
R	Stress ratio

Table 1
Chemical composition of material (wt%).

Material	Al	Si	Ti	V	Fe	Mo
Ti–22V–4Al	4.2	1.0	72.9	21.7	0.2	<0.1

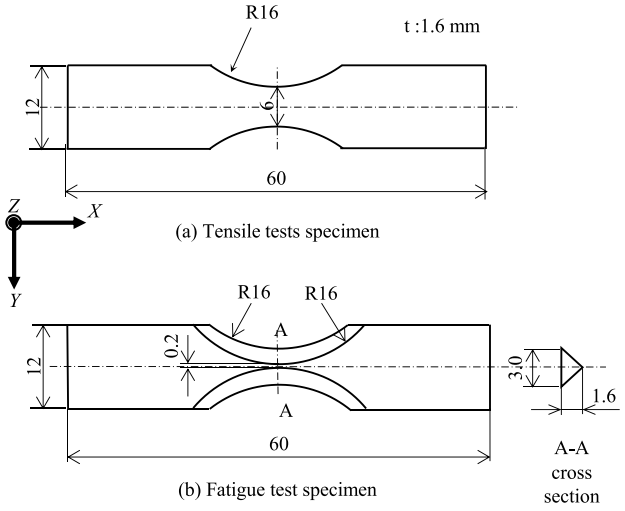

Fig. 1. Schematic illustration of specimen (Ti–22V–4Al).

having high SF values. In addition to these results, many papers [14–20] have discussed the fatigue crack initiation and growth behavior and fractography of many types of titanium alloys.

As mentioned above, extensive research has been conducted on β-type titanium alloys, and their usage is expected to continue expanding in the future. However, there remains an incomplete understanding of fatigue crack initiation in these alloys, particularly in predicting the specific grains within a polycrystalline structure where fatigue cracks will initiate. As mentioned above, the slip systems which generate the fatigue crack should be predicted by using SF parameter, however the grains in polycrystalline where the fatigue crack initiates thought to be not able to be predicted by SF parameter. Therefore, this paper focuses on β-type titanium alloys, anticipated to see broader applications in

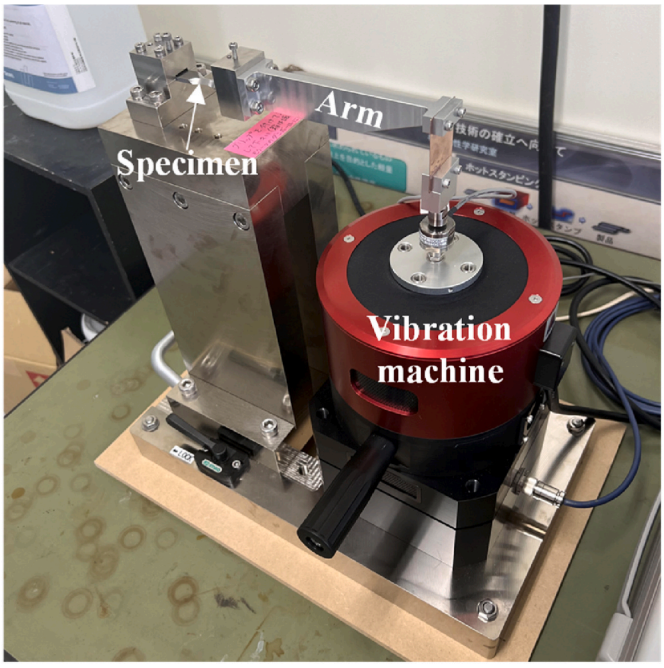

Fig. 2. Plane bending fatigue tests apparatus.

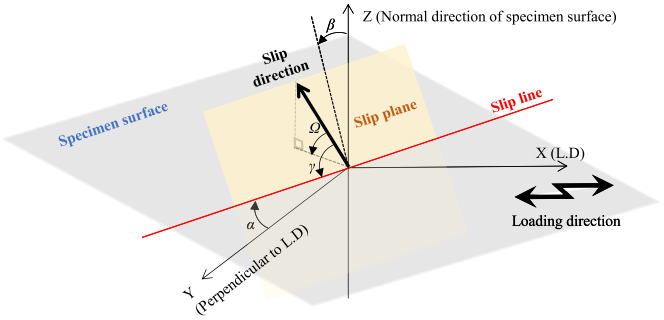

Fig. 3. Definition of axis (X,Y,Z) and slip angles (α,β,γ,Ω).

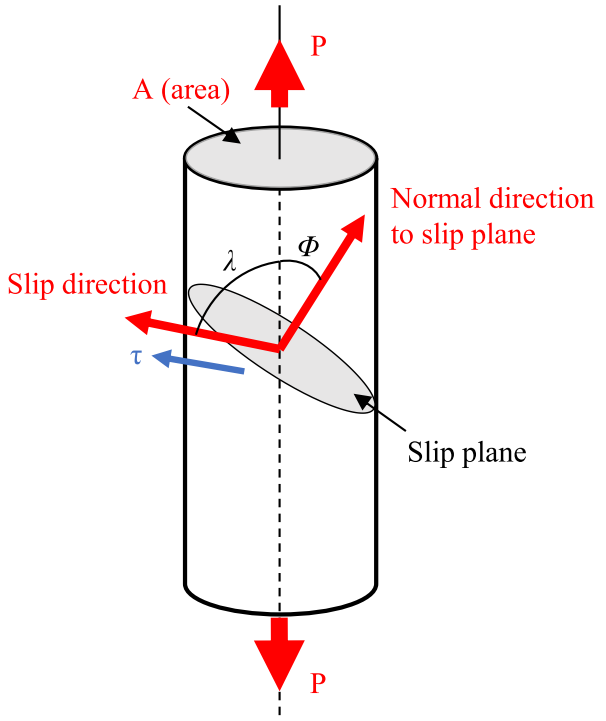

Fig. 4. Calculation of schmidt factor.

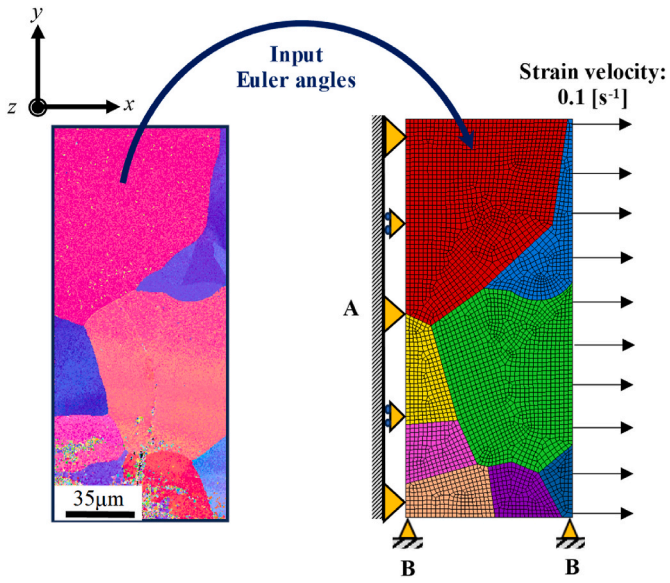

Fig. 5. Typical analysis model and restricted conditions.

precision and small parts, with the aim of enhancing the safety and reliability of parts for long-term use. To achieve this goal, it is conducted that a quantitative evaluation of fatigue crack initiation locations in β-type titanium alloy (Ti–22V–4Al) specimens subjected to plane bending fatigue tests. Furthermore, the aim of our study is to establish the methodologies which let us to be able to predict the fatigue crack initiation sites in polycrystalline. Our investigation specifically considers the driving force such as resolved shear stress. Subsequently, it was employed crystal plasticity finite element analysis (CP-FEM) using crystal orientation data obtained through electron backscatter diffraction (EBSD) analysis. This analysis allowed us to identify potential crystal grains where fatigue cracks may initiate among the polycrystalline grains present on the specimen surface by using the resolved shear stress which express a magnitude of slip activity.

Table 2
Parameters for CP-FEM.

Pan-Rice shear strain increment	
Strain rate sensitivity m	0.01
Reference slip rate	0.001
Hardening modulus k (MPa)	50
n value	0.2
Initial value of CRSS g(α) (MPa)	
{110}<111>	313
Elastic matrix components (GPa)	
c11	140
c12	128
c44	50

2. Exprimental procedure

2.1. Specimen and fatigue tests

In this study, Ti–22V–4Al (DAT51) was used as the test specimen. Table 1 shows the chemical composition of the same material. Fig. 1 (a) and (b) show the shapes of the test specimens used in the tensile test and fatigue test, respectively. The experimental procedure proceeded as follows: Initially, the specimen surface was polished to achieve a mirror-like finish, and the crystal orientation at the center of the R section on one side of the specimen was measured using an EBSD device. Next, to induce fatigue cracks, plane bending fatigue tests were conducted on the specimens. Fatigue cracks occurring on the surface were directly observed using an optical microscope (OM) and indirectly examined using a plastic replica film. The OM facilitated the direct observation of fatigue cracks, while the replica method was used to collect and analyze information regarding the specimen surface to identify the locations of fatigue crack initiation. Upon confirming the occurrence of a fatigue crack through direct observation, the location of the fatigue crack was identified by retracing the surface information obtained via the replica method. The fatigue testing apparatus comprised a vibrator manufactured by Asahi Seisakusho company. As shown in Fig. 2, one side of the test specimen was secured while the other side was attached to the vibrator, enabling controlled vibration of the test specimen under specified load conditions. Furthermore, the conditions for the plane bending fatigue test were as follows: stress amplitude $\sigma_a = 500$ [MPa], stress ratio $R = -0.8$, and repetition frequency $f = 12$ [Hz].

2.2. Expression of slip system

Since the slip system in a crystal grain must be expressed in three dimensions, this study adopts a coordinate system as shown in Fig. 3. Here, the X-axis represents the direction of the load axis on the surface of the specimen, the Y-axis denotes the direction perpendicular to the load axis on the surface, and the Z-axis indicates the direction normal to the surface of the specimen. The slip surface is characterized by the angle α between the slip line occurring on the X–Y plane, as shown in Fig. 3 and the direction perpendicular to the load axis. Additionally, the rotation angle β signifies the deviation of the slip surface concerning the normal direction of the sample surface and the Z-axis. In addition, the slip direction is defined by γ, representing the angle between the slip line and direction. These angles (α, β, and γ) are calculated based on the three-dimensional coordinate information of three points within the crystal structure near the crack tip, where the CI value is relatively high. This information is obtained through crystal orientation analysis using EBSD

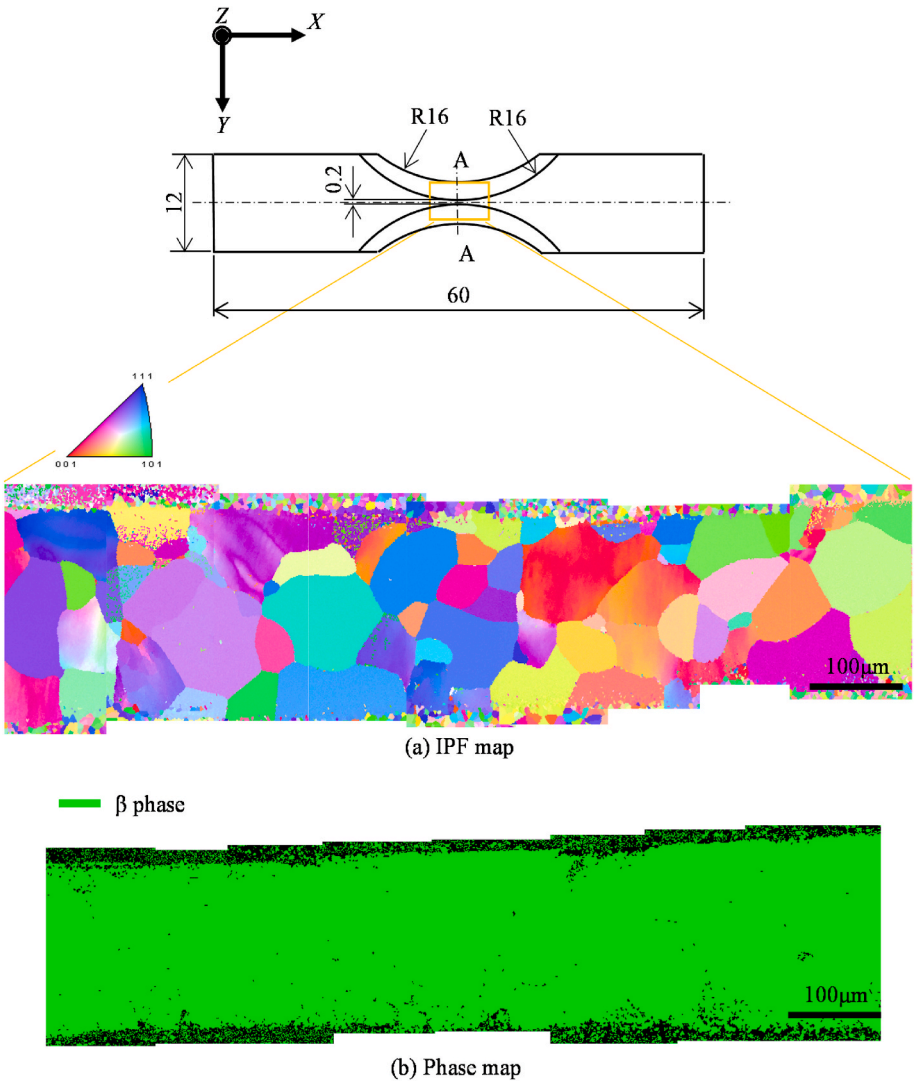

Fig. 6. Microstructure of surface of specimen obtained by using EBSD apparatus.

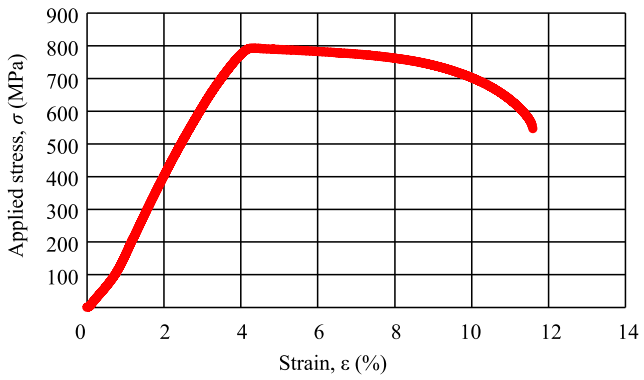

Fig. 7. Stress-Strain curve of Ti–22V–4Al.

results from JEOL JSM-7001F.

2.3. Schmid factor

The shear stress acting in the direction of slip on a slip surface is referred to as the resolved shear stress of the slip system. When a tensile load P is applied to a single crystal round bar with a cross-sectional area A as shown in Fig. 4, the resolved shear stress τ can be expressed as follows [29]:

$$\tau = (P / A) \cdot \cos \Phi \cos \lambda \quad (1)$$

where Φ is defined as the angle between the load axis and the normal direction of the slip surface, and λ is defined as the angle between the load axis and the slip direction. The value of $\cos\Phi\cos\lambda$ in the above equation is referred to as the *Schmid factor* (*SF*). In the case of a crystal with multiple slip systems, the slip system with the largest *SF* becomes the main slip system, which becomes active as the slip system. Furthermore, *SF* was calculated using three-dimensional coordinate information (Euler angles) of crystal orientation obtained through EBSD analysis.

2.4. Theory of crystal plasticity FEM analysis

2.4.1. Constitutive law

In this study, it is adopted a completely implicit method, which can be integrated into the commercial general-purpose finite element method proposed by Kalidindi [21,22]. Based on the formulation outlined above, the following material constitutive law was incorporated as a subroutine program into the general-purpose finite element analysis

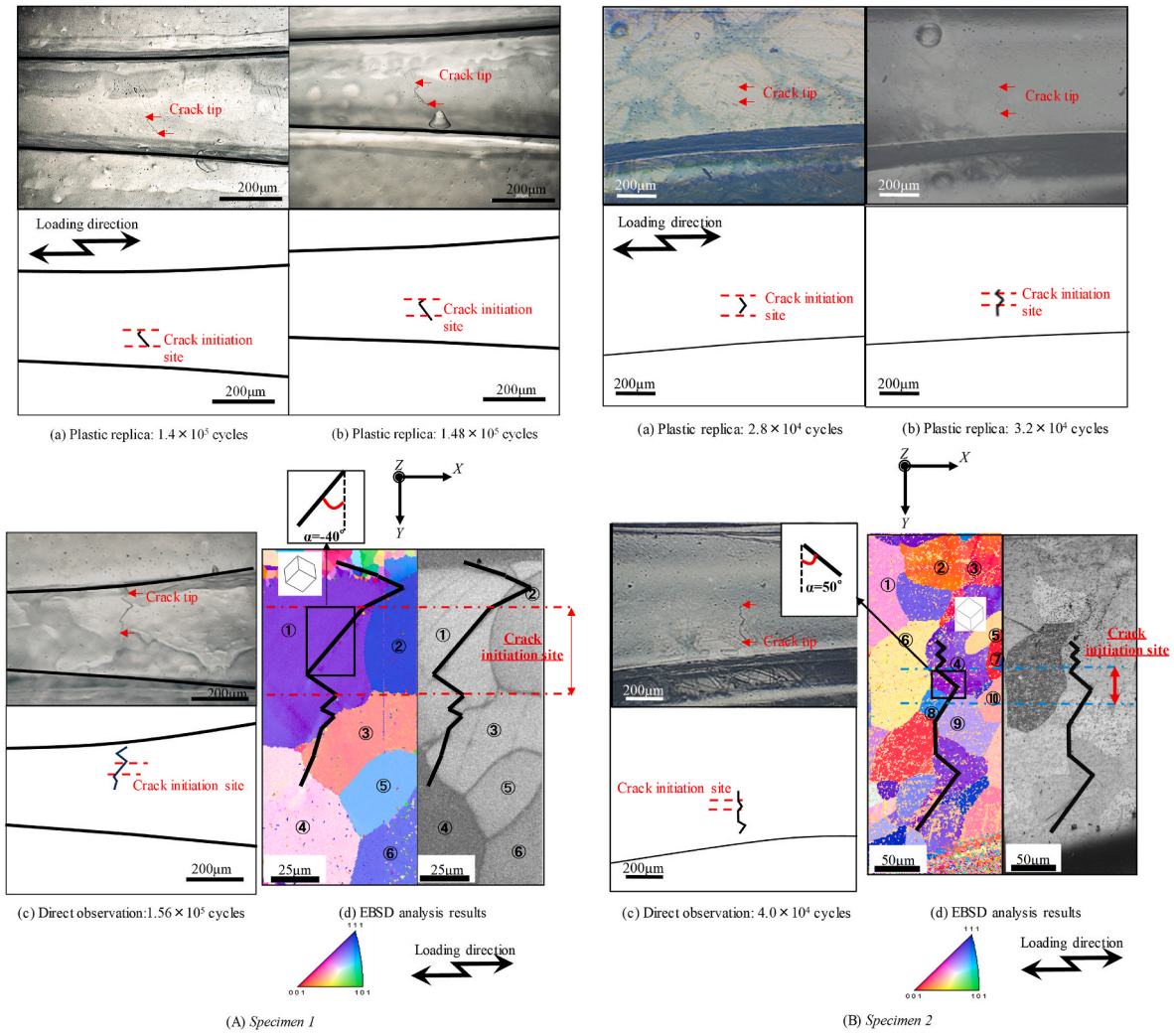

Fig. 8. OM and schematic image of fatigue crack initiation and propagation.

software MSC Marc Mentat (version 2023), enabling stress analysis in accordance with crystal plasticity theory. The elastoplastic decomposition of the deformation gradient tensor $\boldsymbol{F}$, which is essential in crystal plasticity analysis, was performed by extending the crystal plasticity theory initially proposed by Peirce, Asaro, and Needleman [23,24].

$$\boldsymbol{F} = \boldsymbol{F}^{*}\boldsymbol{F}^{p} \tag{2}$$

where $\boldsymbol{F}^{*}$ and $\boldsymbol{F}^{p}$ are the deformation gradient tensors in elastic and inelastic states, respectively. In addition, the plastic deformation gradient tensor $\boldsymbol{F}^{p}$ is represented by the following formula, with the slip system, crucial in crystal slip deformation, being incorporated into the finite element method.

$$\boldsymbol{F}^{p}_{new} = \left(\mathbf{I} - \sum_{\alpha=1}^{N} \dot{\gamma}^{(\alpha)} \boldsymbol{s}_0{}^{(\alpha)} \otimes \boldsymbol{m}_0{}^{(\alpha)}\right) \boldsymbol{F}^{p}_{old} \tag{3}$$

Subsequently, $\boldsymbol{I}$ is the second-order unit tensor, $\boldsymbol{F}^{p}_{new}, \boldsymbol{F}^{p}_{old}$ are the plastic deformation gradient tensors before and after deformation, α is an arbitrary slip system number, N is the total number of slip systems, $\boldsymbol{s}_0{}^{(\alpha)}$ is a unit vector in the slip direction, and $\boldsymbol{m}_0{}^{(\alpha)}$ is a unit vector in the direction normal to the slip surface. To obtain $\dot{\gamma}^{(\alpha)}$, the Pan-Rice type [25] shear strain rate equation provided below was used in the subroutine program.

$$\dot{\gamma}^{(\alpha)} = \dot{\gamma}_0^{(\alpha)} sgn\left(\tau^{(\alpha)}\right) \left|\frac{\tau^{(\alpha)}}{g^{(\alpha)}}\right|^{\frac{1}{m}} \tag{4}$$

Similarly, in the previous equation, α symbolizes an arbitrary slip system, $\dot{\gamma}_0^{(\alpha)}$ is the reference shear strain rate, $\tau^{(\alpha)}$ represents the resolved shear stress (RSS), and $g^{(\alpha)}$ is the critical RSS (CRSS). The evolution law is determined using the Ludwik-type [26] formulation as follows:

$$g^{(\alpha)} = g_0^{(\alpha)} + k\left(\gamma^{(\alpha)}\right)^{n} \tag{5}$$

where $g_0^{(\alpha)}$ denotes the initial value of the CRSS, while k and n represent material parameters characterizing work hardening. The ratio of self-hardening to latent hardening is established at a value of 1.4.

2.4.2. Boundary conditions

The analytical model assigned the Euler angles obtained from EBSD to each crystal grain and replicated the structure surrounding the grain where the fatigue crack occurred. An illustration of the analytical model and its boundary conditions is presented in Fig. 5. A constant strain rate ($\varepsilon_x = 0.1\ s^{-1}$) was applied to the right end face of the analytical model to simulate tensile deformation across the entire metal material. In addition, the displacements were constrained in the X and Z-axis directions on plane A, while displacement was restricted in the Y-axis direction at point B. Table 2 shows the material constants used in the analysis and

Table 3
SF values of grain ① *of Specimen 1*.

Slip System	α [deg]	β [deg]	γ [deg]	Schmidt Factor
(110) [$\bar{1}$11]	46	-29	73	0.271
(110) [1$\bar{1}$1]			60	0.332
($\bar{1}$10) [111]	-51	-13	85	0.040
($\bar{1}$10) [11$\bar{1}$]			25	**0.396**
(011) [11$\bar{1}$]	-2	-61	12	0.072
(011) [1$\bar{1}$1]			59	0.351
(01$\bar{1}$) [$\bar{1}$11]	67	11	81	0.025
(01$\bar{1}$) [111]			28	0.294
(101) [11$\bar{1}$]	-80	41	33	0.117
(101) [$\bar{1}$11]			-38	0.093
($\bar{1}$01) [111]	8	-2	76	0.065
($\bar{1}$01) [1$\bar{1}$1]			6	0.147

Table 4
SF values of grain ④ of *Specimen 2*.

Slip System	α [deg]	β [deg]	γ [deg]	Schmidt Factor
(011) [11$\bar{1}$]	-41	-29	-38	0.362
(011) [1$\bar{1}$1]			-90	0.178
($\bar{1}$01) [111]	-63	11	-27	0.336
($\bar{1}$01) [1$\bar{1}$1]			-82	0.016
(01$\bar{1}$) [$\bar{1}$11]	56	-12	-25	**0.385**
(01$\bar{1}$) [111]			-84	0.020
(110) [$\bar{1}$11]	-15	58	-58	0.290
(110) [1$\bar{1}$1]			-12	0.036
(101) [11$\bar{1}$]	-4	-1	-77	0.036
(101) [$\bar{1}$11]			-6	0.070
($\bar{1}$10) [111]	85	42	37	0.050
($\bar{1}$10) [11$\bar{1}$]			-34	0.056

the initial values of the CRSS in the bcc structure {110}<111> system, referring to the source [26].

3. Experimental results

3.1. Crystal microstructure and tensile test results

Fig. 6 shows the results of the EBSD analysis conducted on the central portion of the specimen. It is evident from this figure that the specimen used in this study comprises crystal grains with a grain size ranging from 100 μm to 200 μm, all of microstructure are β phase. Subsequently, Fig. 7 shows the results of a tensile test conducted using an autograph (manufactured by Shimadzu) at a loading rate of 0.1 kN/s. As observed from Fig. 7, the tensile strength is approximately 800 MPa. Although the tensile strength depends on crystal grain size, this value almost agrees with other results of 967 MPa obtained by G. Xue et al., [30]. In light of this, it is opted to perform cantilever fatigue tests at a maximum stress σ_{max} below this stress value.

3.2. Observation of fatigue crack initiation sites

The conditions for the fatigue test were established based on the tensile test results obtained in the preceding section. Plane bending fatigue tests were executed with a stress amplitude $\sigma_a = 500$ MPa and a stress ratio $R = -0.8$. Fatigue cracks originated from the surface of the specimen, as confirmed through observations made using an optical microscope (OM) and plastic replicas.

3.2.1. Observation of fatigue crack initiation sites

The fatigue crack in Specimen 1 was identified at 1.48×10^5 cycles, and upon tracing back the collected replica images, the cycle count at which the fatigue crack occurred was determined to be 1.4×10^5 cycles. Fig. 8 (a) shows the replica observation results of fatigue crack growth behavior obtained at that juncture. Similarly, Fig. 8(A) and (B) show the observation results of fatigue crack initiation points for Specimens 1 and 2, respectively. These observations confirm the capability to pinpoint fatigue cracks with high accuracy using replica images. Additionally, an EBSD image of the area surrounding the location where the fatigue crack occurred is presented. In the next section, it will be performed that a mechanical evaluation of the fatigue crack initiation sites based on the Euler angles information obtained from EBSD.

3.2.2. Identification of slip system for fatigue crack initiation

Table 3 presents the results of calculating the SF of the {110}<111> system for Specimens 1. From Table 3 it is observed that the maximum Schmid factor of the grains exhibiting crack initiation in Specimen 1 was $SF = 0.396$, and the slip system was ($\bar{1}$10)[11 $\bar{1}$]. The calculated crack initiation angle α_{cal} is −51°, which closely aligns with the experimentally observed α_{exp} of −40°. When calculating α_{cal} for the {112}<111> system, α_{cal} closest value to the experimental α_{exp} of −40°, but $SF = 0.04$, which was a significantly lower value. Also, the maximum Schmid factor

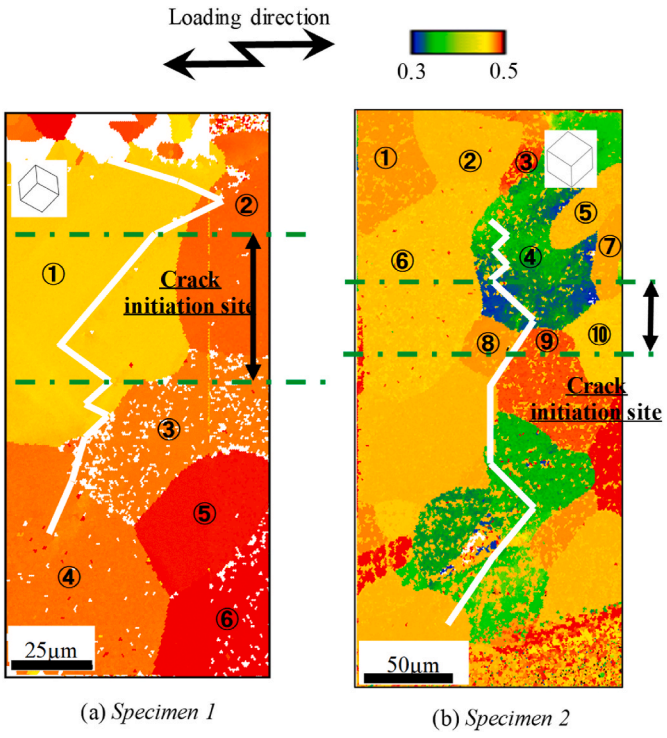

(a) *Specimen 1* (b) *Specimen 2*

Fig. 9. Maximum SF values for each grain around the fatigue crack initiation site.

Table 5
Values of maximum SF for each grain on *specimen 1*.

Grain ID.	*Max. SF*
① Crack initiation	0.396
②	0.447
③	0.391
④	0.465
⑤	0.465
⑥	0.492

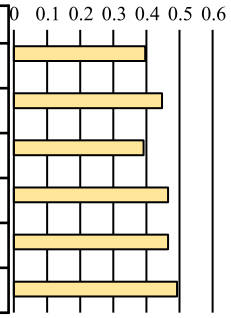

for the {112}<111> system was SF_{max} = 0.498, whose angle of α_{cal} is 85°. However, it is assumed that this slip system did not operate because it was almost parallel to the load axis direction. Therefore, it is considered that the fatigue crack in this specimen was caused by the activity of the slip system $(\bar{1}10)[11\ \bar{1}]$.

Furthermore, regarding Table 4, the maximum SF was 0.385, and the slip system identified was $(01\bar{1})[\bar{1}\ 11]$. Comparing this result with the experimental and calculated values of crack initiation angle α_{cal} 56° and α_{exp} 50° respectively, indicates a reasonable match. In summary, it is evident that the identification of the slip system contributing to fatigue crack initiation can be accomplished based on the magnitude relationship of the SF.

3.2.3. *Identification of crystal grain for fatigue crack initiation*

In the previous section, we successfully identified the slip system contributing to fatigue crack initiation in individual grains. In this section, we aim to ascertain whether it is feasible to identify the crystal grains where fatigue cracks occur by comparing the magnitude relationship of the SF of each grain within a polycrystal using a similar method.

Table 6
Values of maximum SF for each grain on *specimen 2*.

Grain ID.	*Max.SF*
①	0.495
②	0.395
③	0.494
④ Crack initiation	0.385
⑤	0.5
⑥	0.5
⑦	0.5
⑧	0.467
⑨	0.491
⑩	0.486

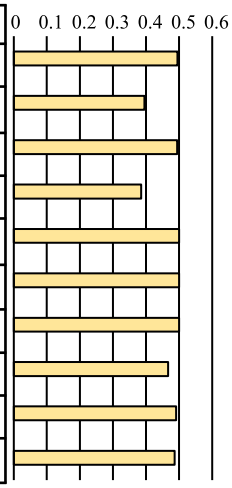

Fig. 9 (a)–(b) show the maximum value of the SF (Max. SF) for each grain of Specimens 1, 2. The numerical values are shown in Table 5. Upon examining Table 5 it becomes apparent that the Schmid factors of other grains are relatively higher than that of grain ①, where fatigue cracks occurred. Therefore, it is inferred that identifying the grains where fatigue cracks occur solely based on the magnitude relationship of the Schmid factor is challenging. Similarly, in Table 6, in addition to grains where fatigue cracks occurred, other grains with high Schmid factors were also identified. This suggests that to identify grains exhibiting fatigue crack initiation, it is imperative to consider the mechanical interaction between grains within a polycrystalline body, as parameters solely based on a single crystal are insufficient.

3.3. *Prediction for fatigue crack initiation sites using CP-FEM*

Since it is imperative to consider a mechanical model of a polycrystalline body to predict fatigue crack initiation sites, it was employed crystal plasticity finite element (CP-FEM) analysis, which accounts for the interaction of slip activities among slip systems and grains. The crystal plasticity analysis model is shown in Fig. 10 (a)–(b). An analytical model was constructed by assigning the Euler angle values of the inverse pole figure map observed via EBSD to each grain, enabling the analytical determination of the RSS acting on the {110}<111> system. Also, boundary conditions are indicated in Section 2.4.2, and mesh sizes of specimen 1, 2 are 4.6 μm and 2.7 μm, respectively. Furthermore, CP-FEM analysis flow is indicated in Fig. 11. The results obtained from the analysis are shown in Fig. 12 (a)–(b). According to Fig. 12 (a), it is evident that the RSS of the $(0\bar{1}1)[111]$ system in grain ① is notably high. In addition, the RSS in the $(0\bar{1}1)[111]$ system was approximately 380 MPa, surpassing that of surround grains whose value are less than 320 MPa. This observation is consistent with Fig. 12 (b), where elevated RSS values are observed for grains exhibiting fatigue crack initiation. As indicated in Fig. 12, the grains having highest resolved shear stress value agree with the fatigue crack initiation points. Therefore, fatigue crack initiation points can be predicted easily by CP-FEM. In essence, it has been elucidated that the onset of fatigue cracks in Ti–22V–4Al materials comprising multiple crystal grains can be predicted by employing CP-FEM analysis of polycrystalline bodies. That's why this numerical analysis method contributes to prediction of fatigue crack initiation sites by considering grain interaction and utilization of resolved shear stress acting each slip system.

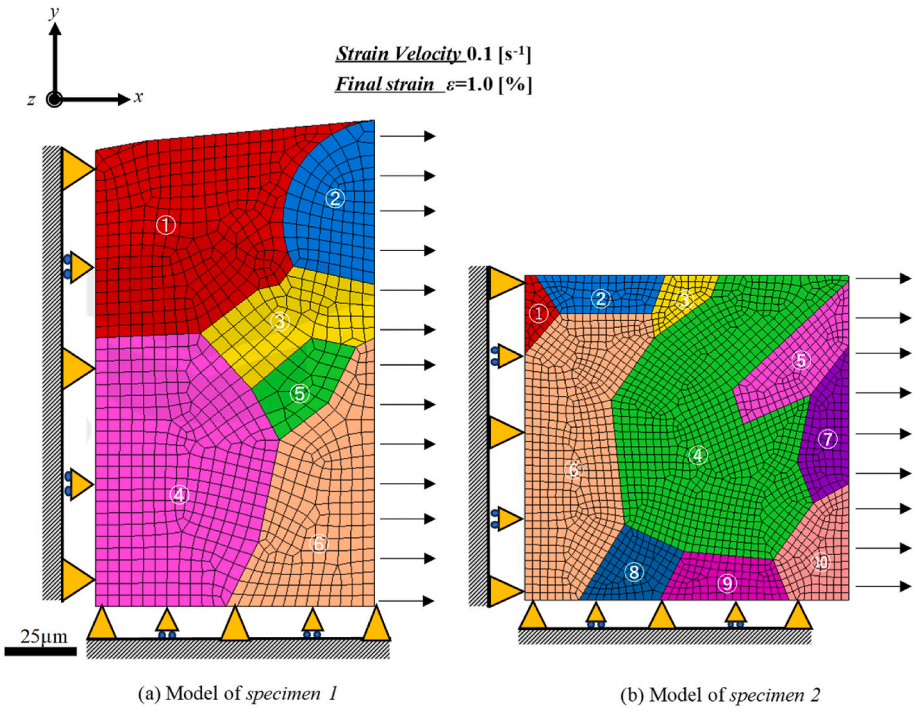

(a) Model of *specimen 1* (b) Model of *specimen 2*

Fig. 10. CP-FEM analysis models for Specimen 1, 2.

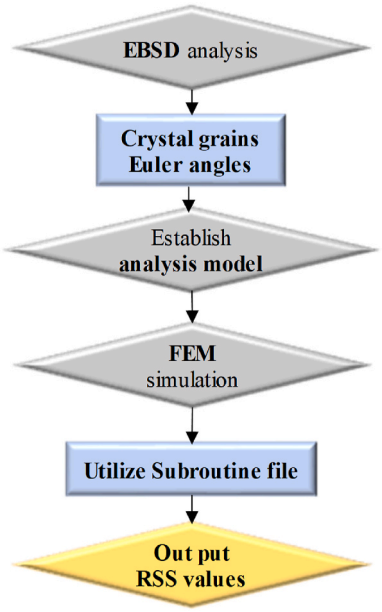

Fig. 11. CP-FEM analysis flow.

3.4. Discussion

In this paper, it has attempted to predict the location of fatigue crack initiation in polycrystals, but it was extremely difficult to identify the location using the Schmidt factor, which is a theory of single crystal plasticity. As mentioned previously [27,28], the slip systems generating the fatigue crack initiation could be predicted by SF and modified SF, however, the fatigue crack initiation sites could be predicted by using these parameters. On the other hand, the CP-FEM can predict the fatigue crack initiation sites in polycrystal. This is because a constant stress σ_∞ acts from a macroscopic perspective when a polycrystal is deformed, but from a microscopic perspective, it depends on the crystal orientation of each crystal grain due to each grain having a different stress by the effect of grain interactions. Therefore, by accurately predicting the resolved shear stress of each slip system of grains through CP-FEM that considers the crystal orientation of polycrystals, it is possible to accurately predict the location of crack occurrence based on quantitatively understanding the amount of slip activity.

4. Conclusion

In this study, plane bending fatigue tests were conducted on Ti–22V–4Al alloy, a β-type titanium alloy, to examine the fatigue crack initiation behavior in detail. In addition, the prediction of fatigue crack initiation points was investigated from the perspectives of the SF and CP-FEM. The key findings of this research are summarized below:

1. The slip system contributing to fatigue crack initiation can be accurately predicted by assessing the magnitude relationship of the SF.
2. Prediction of grains where fatigue cracks will occur can be achieved perfectly in our tested pieces by constructing a crystal plasticity model that considers the mechanical interaction of polycrystals.

CRediT authorship contribution statement

Jinta Arakawa: Writing – review & editing, Writing – original draft, Supervision, Software, Resources, Project administration, Methodology, Investigation, Conceptualization. **Koki Hirazumi:** Investigation, Funding acquisition, Formal analysis, Data curation. **Takeshi Uemori:** Visualization, Validation, Supervision, Software, Resources. **Yoshito Takemoto:** Visualization, Validation, Resources.

Declaration of competing interest

The authors declare that they have no known competing financial interests or personal relationships that could have appeared to influence the work reported in this paper.

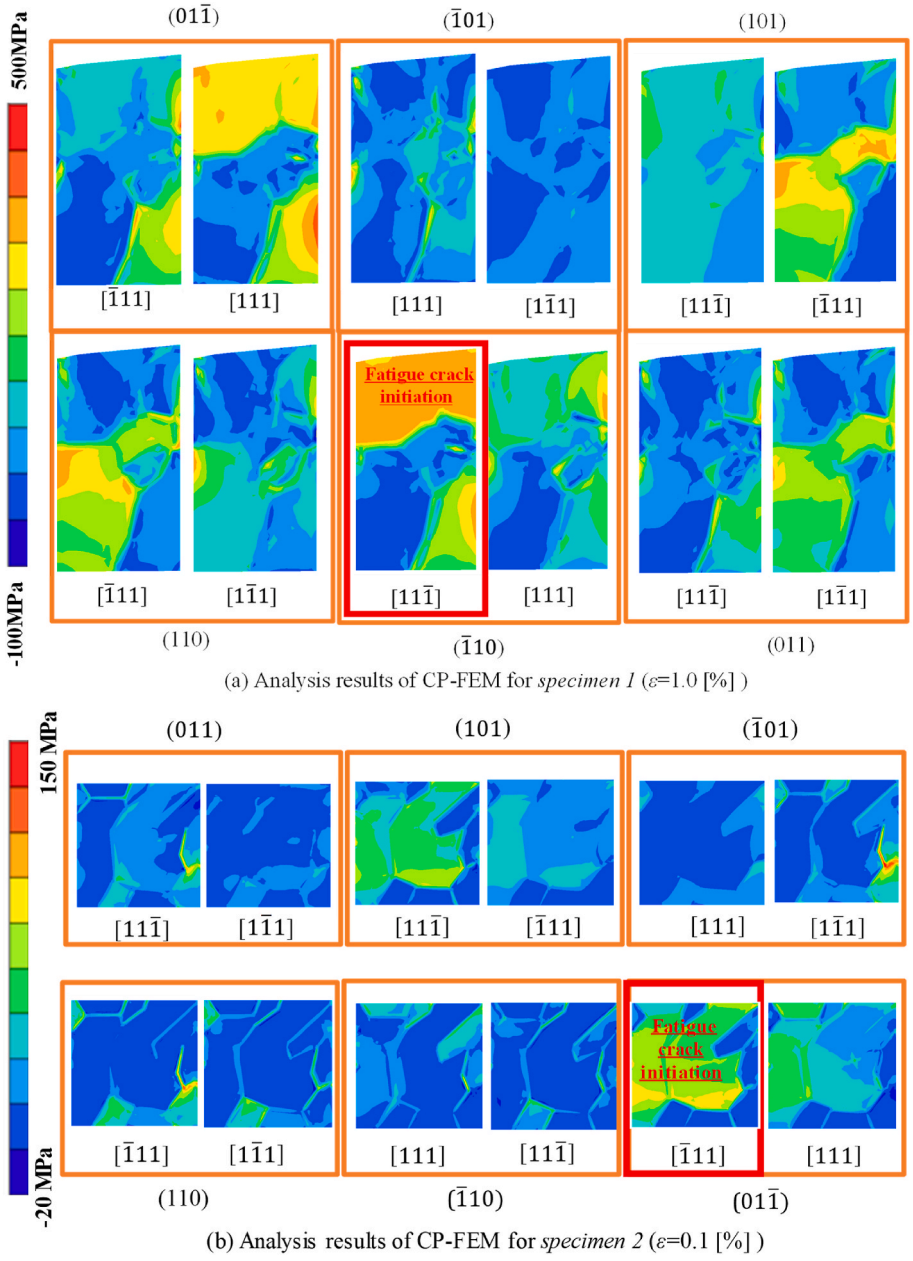

(a) Analysis results of CP-FEM for *specimen 1* (ε=1.0 [%])

(b) Analysis results of CP-FEM for *specimen 2* (ε=0.1 [%])

Fig. 12. Analysis results of Resolved Shear stress (RSS) from CP-FEM for fatigue crack initiation sites for Specimen 1, 2.

Data availability

No data was used for the research described in the article.

References

[1] J.D. Paramore, Z.Z. Fang, M. Dunstan, P. Sun, B.G. Butler, Hydrogen-enabled microstructure and fatigue strength engineering of titanium alloys, Nat Sci Rep 7 (2017) 41444, https://doi.org/10.1038/srep41444.

[2] S. Shina, C. Zhua, C. Zhangb, K.S. Vecchio, Extraordinary strength-ductility synergy in a heterogeneous-structured β-Ti alloy through microstructural optimization, Mater Res Lett 7 (2019) 467–473, https://doi.org/10.1080/21663831.2019.1620156.

[3] A. Cox, S. Herbert, J.P. Villain-Chastre, S. Turner, M. Jackson, The effect of machining and induced surface deformation on the fatigue performance of a high strength metastable titanium alloy, Int. J. Fatig. 19 (2019), https://doi.org/10.1016/j.ijfatigue.2019.30053-2, 30053–2.

[4] L.C. Campanelli, A review on the recent advances concerning the fatigue performance of titanium alloys for orthopedic applications, J. Mater. Res. 36 (2021) 151–165, https://doi.org/10.1557/jmr.2021.151.

[5] W. Zhu, J. Lei, C. Tan, Q. Sun, W. Chen, L. Xiao, J. Sun, A novel high-strength β-Ti alloy with hierarchical distribution of α-phase: the superior combination of strength and ductility, Mater. Des. 168 (2019) 107640, https://doi.org/10.1016/j.matdes.2019.107640.

[6] P. Pesode, S. Barve, A review—metastable β titanium alloy for biomedical applications, J. Eng. Appl. Sci. 70 (2023) 25, https://doi.org/10.1007/s13369-022-06625-8.

[7] R.Z. Valiev, E.A. Prokofiev, N.A. Kazarinov, G.I. Raab, T.B. Minasov, J. Stráský, Developing nanostructured Ti alloys for innovative implantable medical devices, Materials 13 (2020) 967, https://doi.org/10.3390/ma13040967.

[8] B.B. Straumal, A.S. Gornakova, A.R. Kilmametov, E. Rabkin, N.Y. Anisimova, M. V. Kiselevskiy, β-Ti-based alloys for medical applications, Phys Metall Heat Treat 6 (2020) 52–64, https://doi.org/10.1007/s11041-020-00552-7.

[9] W. Chen, Y.C. Lin, X. Zhang, K. Zhou, Balancing strength and ductility by controllable heat-treatment twinning in a near β-Ti alloy, J. Mater. Res. Technol. 9 (2020) 6962–6968, https://doi.org/10.1016/j.jmrt.2020.05.003.

[10] N. Yumak, K. Aslantas, A review on heat treatment efficiency in metastable β titanium alloys: the role of treatment process and parameters, J. Mater. Res. Technol. 9 (2020) 15360–15380, https://doi.org/10.1016/j.jmrt.2020.10.086.

[11] K. Tokaji, T. Ogawa, K. Ohya, The effect of grain size on small fatigue crack growth in pure titanium, Int. J. Fatig. 16 (1994) 571–578, https://doi.org/10.1016/0142-1123(94)90011-6.

[12] H. Proudhon, J. Li, W. Ludwig, A. Roos, S. Forest, Simulation of short fatigue crack propagation in a 3D experimental microstructure, Adv. Eng. Mater. 19 (2017) 1600721, https://doi.org/10.1002/adem.201600721.
[13] M.Y. Abdellah, H. Alharthi, Fracture toughness and fatigue crack growth analyses on a biomedical Ti-27Nb alloy under constant amplitude loading using extended finite element modelling, Materials 16 (2023) 4467, https://doi.org/10.3390/ma16094467.
[14] P. Xu, F. Pyczak, W. Limberg, R. Willumeit-Römer, T. Ebel, Superior fatigue endurance exempt from high processing cleanliness of metal-injection-molded β Ti-Nb-Zr for bio-tolerant applications, Mater. Des. 211 (2021) 110141, https://doi.org/10.1016/j.matdes.2021.110141.
[15] L.M. Young, G.A. Young, J.R. Scully, et al., Aqueous environmental crack propagation in high-strength beta titanium alloys, Metall. Mater. Trans. A 26 (1995) 1257–1271, https://doi.org/10.1007/BF02670620.
[16] P. Schmidt, A. El-Chaikh, H.J. Christ, Effect of duplex aging on the initiation and propagation of fatigue cracks in the solute-rich metastable β titanium alloy Ti 38-644, Metall. Mater. Trans. A 42 (2011) 2652–2667, https://doi.org/10.1007/s11661-011-0662-7.
[17] A. Cremasco, E.S.N. Lopes, F.F. Cardoso, R.J. Contieri, I. Ferreira, R. Caram, Effects of the microstructural characteristics of a metastable β Ti alloy on its corrosion fatigue properties, Int. J. Fatig. 54 (2013) 32–37, https://doi.org/10.1016/j.ijfatigue.2013.04.018.
[18] J. Kumar, V. Singh, P. Ghosal, V. Kumar, Characterization of fracture and deformation mechanism in a high strength beta titanium alloy Ti-10-2-3 using EBSD technique, Mater. Sci. Eng., A 623 (2015) 49–58, https://doi.org/10.1016/j.msea.2014.11.021.
[19] Young Somerday, Gangloff. Crack tip mechanics effects on environment-assisted cracking of beta-titanium alloys in aqueous NaCl, Fatig. Fract. Eng. Mater. Struct. 23 (2000) 39–58, https://doi.org/10.1046/j.1460-2695.2000.00243.x.
[20] Z. Wu, H. Kou, N. Chen, K. Hua, M. Zhang, J. Fan, B. Tang, J. Li, The effects of grain morphology and crystallographic orientation on fatigue crack initiation in a metastable β titanium alloy Ti-7333. https://doi.org/10.1016/j.msea.2020.140222, 2020.
[21] S.R. Kalidindi, Incorporation of deformation twinning in crystal plasticity models, J. Mech. Phys. Solid. 46 (267–71) (1998) 273–290, https://doi.org/10.1016/S0022-5096(97)00081-X.
[22] S.R. Kalidindi, H.K. Duvvuru, M. Knezevic, Spectral calibration of crystal plasticity models, Acta Mater. 54 (2006) 1795–1804, https://doi.org/10.1016/j.actamat.2005.12.016.
[23] R.J. Asaro, A. Needleman, Overview no. 42 Texture development and strain hardening in rate dependent polycrystals, Acta Metall. 33 (1985) 923–953, https://doi.org/10.1016/0001-6160(85)90132-8.
[24] J. Lemonds, R.J. Asaro, A. Needleman, A numerical study of localized deformation in bi-crystals, Mech. Mater. 4 (1985) 417–435, https://doi.org/10.1016/0167-6636(85)90016-3.
[25] J. Pan, J.R. Rice, Rate sensitivity of plastic flow and implications for yield-surface vertices, Int. J. Solid Struct. 19 (1983) 973–987, https://doi.org/10.1016/0020-7683(83)90054-3.
[26] M. Demiral, K. Nowag, A. Roy, R. Ghisleni, J. Michler, V.V. Silberschmidt, Enhanced gradient crystal-plasticity study of size effects in a β-titanium alloy, Model. Simulat. Mater. Sci. Eng. 25 (2017) 035013, https://doi.org/10.1088/1361-651X/aa5b4f.
[27] C. Liu, X. Xu, T. Sun, R. Thomas, J. Quinta da Fonseca, M. Preuss, Microstructural effects on fatigue crack initiation mechanisms in a near-alpha titanium alloy, Acta Mater. 253 (2023) 118957, https://doi.org/10.1016/j.actamat.2023.118957.
[28] F. Meng, R. Zhang, S. Wang, F. Sun, R. Chen, L. Huang, Fatigue crack initiation and propagation dominated by crystallographic factors in TiB/near α-Ti composite, Acta Metall. Sin. 37 (2024) 763–776, https://doi.org/10.1007/s40195-024-01677-1.
[29] K. Wang, Z. Yan, Y. Zhou, S. Wei, X. Wang, R. Xin, Q. Liu, Slip initiation in interlayered β and corresponding slip transfer during compression of a lamellar-structure titanium alloy, Results Phys. 18 (2020) 103276, https://doi.org/10.1016/j.rinp.2020.103276.
[30] G. Xue, T. Nakamura, N. Fujimura, K. Takahashi, H. Oguma, A. Takeuchi, M. Uesugi, K. Uesugi, Initiation and propagation of small fatigue crack in beta titanium alloy observed through synchrotron radiation multiscale computed tomography, Eng. Fract. Mech. 263 (2022) 108308, https://doi.org/10.1016/j.engfracmech.2022.108308.